RSC Advances

ROYAL SOCIETY OF CHEMISTRY

www.rsc.org/advances

Journal Name

RSCPublishing

ARTICLE

Synthesis of Bi_2WO_6 Photoanode on Transparent Conducting Oxide Substrate with Low Onset Potential for Solar Water Splitting

Cite this: DOI: 10.1039/x0xx00000x

Received 00th January 2012,
Accepted 00th January 2012

DOI: 10.1039/x0xx00000x

www.rsc.org/

Sang Youn Chae[a,b], Eun Seon Lee[a], Hyejin Jung [a,c], Yun Jeong Hwang[a,c]*, and Oh-Shim Joo[a]*,

To enable water splitting in photoelectrochemical cells, the conduction-band (CB) and valence-band edges must straddle the hydrogen-reduction and water-oxidation potentials; however, the CB edge potential of many photoanodic semiconductors is insufficient. Here, we demonstrate the nanostructured Bi_2WO_6 for photoanodic application of, which has a high, flat-band potential of 0.15 V *vs.* RHE. Single-phase, orthorhombic Bi_2WO_6 nano-structures were successfully grown on an FTO substrate through a two-step hydrothermal synthesis with subsequent thermal treatment at 600 °C. The synthesized Bi_2WO_6 photoanode shows a lower onset potential and improved photocurrents which were enhanced further by a factor of three by coating the surface with Co-Pi. The low onset potential of the Bi_2WO_6/Co-Pi photoanode results in the higher operating photocurrent in a p/n photodiode cell combined with a p-Si/n-Si/Pt photocathode.

1. Introduction

The economic, political, and environmental issues related to fossil fuels are expediting the global interest regarding the conversion of solar energy to fuel to aid in the development of renewable energy resources.[1, 2] In this method of fuel-production, solar energy is converted and stored in chemical bonds by transferring photo-excited charge carriers to chemical oxidation/reduction reactions. For example, in a photoelectrochemical (PEC) water-splitting system, a semiconductor material absorbs sunlight, generates charge carriers, and then catalyzes hydrogen/oxygen evolution reactions using the excited charge carriers. Because the semiconductors play multiple roles, ideal semiconductors must satisfy several requirements,[3, 4] and the preparation of photoelectrodes containing the semiconductors is critical to maximizing their photocatalytic performances.[5]

Metal-oxide semiconductors, such as TiO_2,[6] WO_3,[7, 8] and Fe_2O_3[9-11], have been intensively studied for PEC water-splitting due to their high chemical stability and synthetic feasibility. However, the low conduction-band (CB) edge positions of metal oxides relative to the hydrogen reduction potential are disadvantageous for water splitting. For example, the valence band (VB) of WO_3 has sufficiently low energy (~3.0 V *vs*. NHE) to oxidize water, but its low CB edge (~0.3 V *vs*. NHE) thermodynamically prohibits spontaneous hydrogen reduction.[12, 13] This drawback encourages research into the development of new types of metal-oxide semiconductors with higher CB edges.

Bi_2WO_6, which is a ternary oxide, has been reported to have a CB that is closer to the hydrogen reduction potential and higher than that of WO_3.[14] The bandgap of Bi_2WO_6 is ~2.7–2.8 eV, which is slightly larger than that of WO_3 (~2.6–2.7 eV); this larger bandgap boosts the CB potential.[15, 16] Therefore, a Bi_2WO_6 photoanode can split water without or with a small applied bias potential, and its combination with another p-type semiconductor, such as a p/n photodiode system, enables overall water splitting. The earlier PEC studies regarding Bi_2WO_6 focused on the photodegradation of environmental pollutants and powder-type approaches that did not involve the fabrication of an electrode.[17-23] Only few recent studies regarding PEC water-splitting using an electrode-based approach,[14, 24] which can measure improved PEC properties, including the onset potential for water oxidation and a flat-band potential related to the CB position, have been reported.

In this report, we describe the hydrothermal synthesis of nanostructured Bi_2WO_6 directly onto an FTO substrate for photoanode applications. The intermediate $WO_3 \cdot 0.33H_2O$ nanorod film was converted to Bi_2WO_6 during the second hydrothermal reaction. The photocurrents and onset potentials of the anodic photocurrent are discussed with respect to the annealing conditions and deposition of cobalt phosphate (Co-Pi) as an oxygen evolution catalyst. After loading Co-Pi onto the Bi_2WO_6 electrode surface, the water oxidation dynamics improved and the onset potential (0.15 V *vs*. RHE) decreased down to a flat-band potential, which was measured using the Mott-Schottky measurement method.

2. Experimental Section

A two-step hydrothermal reaction was applied to synthesize Bi_2WO_6. Firstly, tungsten oxide nanorods were prepared directly on an FTO substrate[8] and then converted to Bi_2WO_6 in the presence of a Bi precursor. Ammonium paratungstate pentahydrate ($(NH_4)_{10}W_{12}O_{41}\cdot 5H_2O$; 1 g) (Alfa Aesar, 99.999%) was dissolved in distilled water (93 mL) and stirred for 1 h before the addition of HCl (3 mL, Sigma Aldrich, 37.5%). After stirring for 30 min, 4 mL of H_2O_2 (Junsei, 30%) was added and the mixture was stirred for an additional 1.5 h. This tungsten precursor solution was transferred to a Teflon liner and a clean FTO substrate was placed face-down in the solution for the duration of the hydrothermal reaction at 160 °C (4 h). The reaction resulted in the growth of $WO_3\cdot 0.33H_2O$ nanorods on the FTO side, which was then rinsed with water. The second hydrothermal reaction was conducted in a 0.1 mM $Bi(NO_3)_3\cdot 5H_2O$ (Sigma Aldrich, 98%) aqueous solution at 160 °C for 24 h with the as-prepared $WO_3\cdot 0.33H_2O$ film or with the

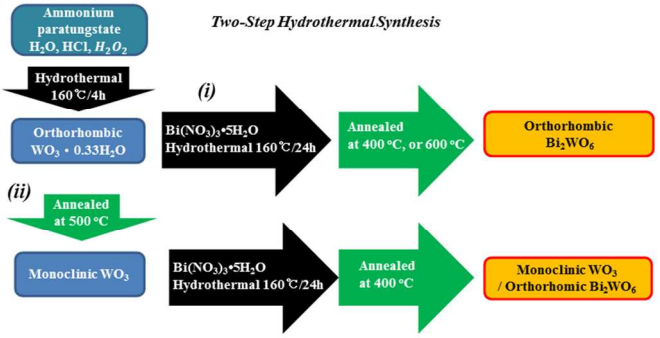

500 °C for 2 h annealed film. After the second reaction, the film was rinsed and annealed at 400–800 °C for 4 h. Scheme 1 shows the overall synthesis.

Scheme 1. Bi_2WO_6 synthetic strategy with crystal structures obtained at each step.

Co-Pi was deposited on the Bi_2WO_6 surface by electrodeposition using a three-electrode system.[25, 26] The electrolytic bath comprised 0.1 mM $CoCl_2\cdot 6H_2O$ (Sigma Aldrich, 98%) in a 0.1 M potassium phosphate buffer solution, and 1.1 V *vs.* Ag/AgCl was applied for 15 min using a potentiostat (Iviumstat, Ivium Technology).

PEC performances were measured in a 0.5 M Na_2SO_4 aqueous solution using linear sweep voltammetry at a rate of 20 mV/s under simulated one-sun illumination (100 mW/cm^2), which was generated from a solar simulator (ABET, Sun 2000) equipped with 300 W Xe lamp and 1.5 air mass filter. The measurements were carried out using a three-electrode system with an Ag/AgCl reference electrode, a Pt counter electrode, and the synthesized films as the working electrode. Mott-Schottky measurements were performed to measure the flat-band potential of the synthesized Bi_2WO_6 electrode in a 0.5 M Na_2SO_4 aqueous solution. The potential was scanned from 0.0 to 0.6 V *vs.* RHE (potential amplitude of 50 mV) with two different frequencies, i.e., 0.5 and 1.0 kHz, to minimize the effects of the surface states.

An operating current of the overall water splitting was measured by linking the Bi_2WO_6 photoanode with a silicon photocathode under simulated sunlight illumination. p-Si photocathode was prepared from Si (111) substrate (boron doped, 0.1~0.3 Ωcm resistivity), and Pt was deposited on the Si electrode by electrochemical deposition under illumination with 0.04M H_2PtCl_4 (Aldrich) precursor solution.[27] To shift the onset potential of Si photocathode toward anodic direction, p-Si/n-Si junction was formed by doping with phosphorous on the surface of the p-Si substrate as Boettcher *et al.* reported.[28] Spin on phosphorous dopant (Filmtronics, P509) solution was coated on the HF cleaned p-Si substrate by spin coating at 2000 rpm followed by baking at 150 °C, and annealing at 950 °C for 1hr. After the annealing, spin on dopant was removed by etching in buffered HF solution (Aldrich) before Pt electrodeposition. I-V curves of the p-Si/Pt and p-Si/n-Si/Pt photocathodes were measured similarly to Bi_2WO_6 photoanode. The only difference was that linear sweep voltammetry was applied to cathodic direction (from 0.8 V to -0.5 V vs RHE).

Scanning electron microscopy (SEM; S-4100, Hitachi) was used to investigate the surface morphology of the hydrothermally synthesized films, and the crystal structures were characterized using X-ray diffraction (XRD, Schimadzu X). The absorbance was measured using UV-vis spectrometer (Varian, Cary 100).

3. Result and discussion

The morphologies of the nanostructured films varied during each step of hydrothermal growth and annealing according to the SEM images (Figure 1). Rod-like nanostructures were observed after the first hydrothermal growth (Figure 1a); these transformed to a flower-like morphology during the second hydrothermal reaction with the Bi precursor and annealing at 400 °C (Figure 1b). A smoother surface was obtained with annealing at 600 °C (Figures 1c–d) and EDS elemental analysis confirmed a Bi/W atomic ratio of 2:1. (Figure S1) On the other hand, annealing the as-prepared film in the first hydrothermal growth (Figure 1a) at 500 °C prior to the second reaction results in smoother rod-like structures (Figure 1e); these nanostructures break down to smaller sizes after the second hydrothermal reaction and subsequent annealing at 400 °C (Figure 1f).

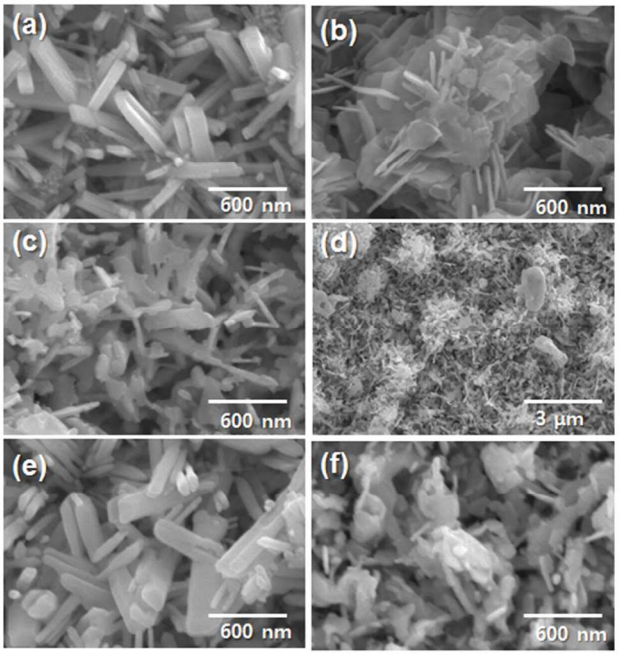

Figure 1. SEM images of (a) as-grown nanorod arrays after the first hydrothermal reaction (orthorhombic $WO_3\cdot 0.33H_2O$) and samples annealed (b) at 400 °C, and (c),(d) at 600 °C after the second hydrothermal synthesis (orthorhombic Bi_2WO_6) ((d) shows a lower magnification). SEM images of samples annealed (e) at 500 °C after the first hydrothermal reaction (monoclinic WO_3) and (f) at 400 °C (mixture

of monoclinic WO_3 and orthorhombic Bi_2WO_6) after the second hydrothermal synthesis using sample (e).

Although the morphologies of the films are different, the films adhere stably to the FTO substrates even after the second hydrothermal growth and subsequent annealing. During the first hydrothermal reaction, the *in situ* formation of a seed layer on the FTO substrate is evident initially, i.e., after less than 1 h, and the rod-like structures grow on top of the seed layer, which results in good adhesion.[8]

An attempt to grow Bi_2WO_6 via a one-pot hydrothermal reaction failed to result in the formation of only orthorhombic WO_3 H_2O film on the FTO substrate (Supporting Information Figures S3 and S4) due to the unbalanced reactivity of the W and Bi precursors. SEM-EDS showed that a negligible amount of Bi is included in the final film although the morphology and crystal structure of the hydrated tungsten oxide are affected by the presence of the Bi precursor. This unsuccessful synthesis of Bi_2WO_6 guided us to design a two-step hydrothermal synthesis to introduce Bi into the crystal structure of tungsten oxide during a second step of growth at 160 °C for 24 h.

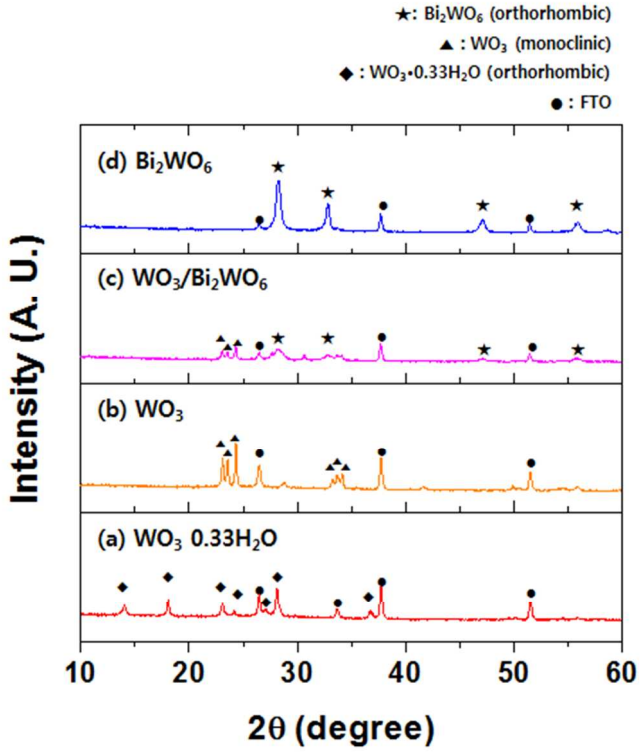

Figure 2. XRD spectra of the prepared sample at each step showing complete conversion of WO_3·0.33H_2O to Bi_2WO_6 and partial conversion of monoclinic WO_3 to WO_3/Bi_2WO_6 during the second hydrothermal reaction.

An orthorhombic Bi_2WO_6 nanostructured film can be synthesized directly onto the FTO substrate using a two-step hydrothermal approach in which an orthorhombic WO_3 0.33 H_2O nanorod film is successfully converted, as evident from the XRD spectra (Figure 2). After the first hydrothermal growth with only the tungsten precursor, the sample has an orthorhombic WO_3 0.33 H_2O crystal structure[8] (Figure 2a), which converts to a monoclinic WO_3 structure upon annealing at 500 °C in air (Figure 2b). Complete conversion to Bi_2WO_6 was only observed (Figure 2d) when the second hydrothermal reaction was performed using the as-prepared sample; the crystal structure of the orthorhombic Bi_2WO_6 did not change even with the post-annealing (Figure S5). A mixture of WO_3 and Bi_2WO_6 was obtained (Figure 2c) when the second hydrothermal reaction was carried out using the annealed monoclinic WO_3 nanorod film, which indicates the partial inclusion of Bi into the tungsten oxide crystal structure. The relatively weak interactions between adjacent layers in the orthorhombic WO_3 0.33 H_2O crystal structure make it more susceptible to attack by Bi^{3+} than the thermodynamically stable monoclinic WO_3.[8] We used pure samples of Bi_2WO_6 resulting from the two-step hydrothermal synthesis for the following photocatalytic analyses.

The photocurrent of the Bi_2WO_6 photoanodes strongly depends on the post-annealing conditions. The sample annealed at 600 °C has the highest photocurrent (Figure 3a). The prepared Bi_2WO_6 photoanodes were applied to photo-oxidation of water in a 0.5 M Na_2SO_4 aqueous solution post annealing at 500, 600, and 800 °C, respectively. The sample was annealed at 800 °C for only 10 min because of the thermal stability of the FTO substrate, while the others were annealed for 1 h in air. The solid lines in Figure 3a represent the photocurrent under simulated sunlight conditions, while the dotted lines show the current in the dark. The photocurrents (at 1.23 V *vs.* RHE) of the Bi_2WO_6 photoanodes annealed at 500, 600, and 800 °C are 5.55, 11.3, and 8.5 μA/cm^2, respectively; thus, the photocurrent of the sample annealed at 600 °C is almost twice that of the sample annealed at 500 °C. In addition, a dramatic change in the slope of the photocurrent versus the bias potential (Figure 3a) is observed when Bi_2WO_6 is annealed above 600 °C. The morphology changes or the enhanced crystalline structures may contribute to the higher activities of the high temperature-annealed samples. Although the FTO substrate is known to be stable up to 650 °C,[29] the effect of the thermal stability of FTO on the reproducibility of the photocurrent is a concern after annealing at high temperatures such as 800 °C, and decreased electrical conductivity of the FTO substrate can cause a lower photocurrent despite a lower onset potential.

The photocurrent of the Bi_2WO_6 electrode was enhanced by a factor of three (~30 μA/cm^2) upon deposition of Co-Pi, which is known to be an efficient electro-catalyst for the oxygen evolution reaction (OER). In particular, the photocurrent was improved under positively biased conditions with a high fill-factor, as shown in the *I–V* curves. (Figure 3b) A previous study regarding Bi_2WO_6 also reported a poor photocurrent level in the order of few tens of μA/cm^2,[15, 16, 24] which is low considering the reported bandgap of ~2.7–2.9 eV and our UV-vis absorption data (Figure 4b). Therefore, the low photocurrent levels are suspected to be due to poor charge collection efficiency which can be caused by insufficient charge transport within the semiconductor material and/or insufficient charge transfer across the semiconductor and electrolyte interface. The former is related to the material properties, such as charge–carrier mobility, depletion width, etc., while the latter is also related to the catalytic activity on the surface of the semiconductor. The influence of the OER catalyst loading on the photocurrent is significant if the oxidation activity on the semiconductor is poor. Co-Pi has been demonstrated to be a good OER catalyst material on a $BiVO_4$ photoanode in which poor water-oxidation activities obstruct charge separation at the semiconductor surface.[26, 30] Here, we demonstrate that a Co-Pi layer can also enhance water oxidation activity of the Bi_2WO_6 photoanode, meaning the poor water oxidation activity is one of the reasons to show low level of photocurrent with Bi_2WO_6.

The electrodeposited Co-Pi layer is expected to be effectively coated onto the nanostructured Bi_2WO_6 surface and can facilitate charge transfer at the Bi_2WO_6/electrolyte interface.

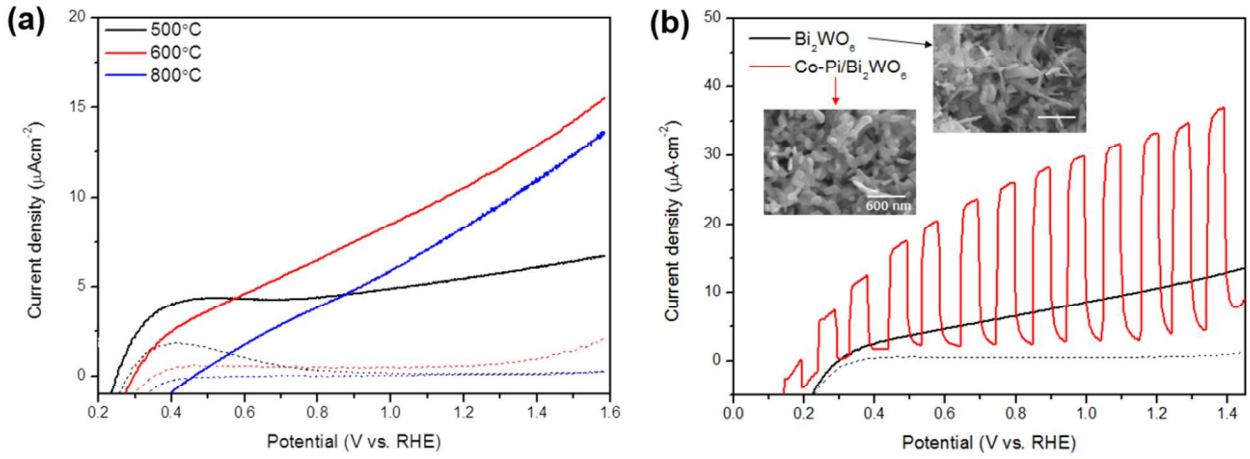

Figure 3. (a) Photoanodic current densities *vs.* RHE with varying annealing temperatures (solid line: under simulated sunlight illumination, dotted line: in dark), and (b) enhanced photocurrent densities upon Co-Pi deposition. (red line shows photocurrent under the chopped illumination)

The onset potential of the Co-Pi/Bi_2WO_6 photoanode is around +0.15 V *vs.* RHE (Figure 3b), which is much lower than those of Fe_2O_3 (+0.8 V *vs.* RHE) and WO_3 (+0.5 V *vs.* RHE).[3] Its flat-band potential (E_{fb}) was determined to be 0.15 V *vs.* RHE through Mott-Schottky measurements (Figure 4a) at 0.5 and 1.0 kHz. Using the following equation, E_{fb} can be determined from the x-intercept value:

$$\frac{1}{C_{sc}^2} = \frac{2}{\varepsilon\varepsilon_0 A^2 e N_D}\left(E - E_{fb} - \frac{kT}{e}\right),$$

where C_{sc} is the space charge capacitance, ε is the dielectric constant of the semiconductor, ε_0 is the permittivity of free space, N_D is the carrier concentration, A is the surface area of the electrode, E is the applied potential, k is the Boltzmann constant, and T is the temperature. The onset potential is well matched with the observed flat-band potential when Co-Pi is deposited. The bandgap of the prepared Bi_2WO_6 is ~2.7 eV according to UV-vis measurements (Figure 4b), which is slightly wider than that of monoclinic WO_3 (~2.6 eV); these results are consistent with those of previous studies[14] and suggest that the CB positions of Bi_2WO_6 are at a more positive potential than those of monoclinic WO_3. The shift direction is preferable for overall water splitting.

Notably, lowering the onset potential of the Bi_2WO_6 photoanode is promising for the realization of spontaneous water splitting in a composite PEC system, such as a p/n photodiode PEC cell or photovoltage cell-combined tandem PEC cell.[31, 32] In these PEC systems, the operating photocurrent is determined from the overlap of the I–V curves, which means that the currents (or charge flows) must be balanced on the cathodic and anodic sides. Therefore, lowering the onset potential is important to obtain high operating photocurrents because most of the onset potentials of n-type semiconductors are generally too high to cross the I–V curves of p-type semiconductors. For example, the onset potential of a p-type Si photocathode,[33] which is one of the popular semiconductors for hydrogen producing photo-cathodes, is known to be +0.3 V vs. RHE. Its onset potential can shift anodically up to 0.55 V vs. RHE by forming n+p Si junction [28], but it is too cathodic to couple effectively with photoanodes such as WO3 and Fe2O3. The overlap of the IV curves either does not occur or occurs at a negligible current level. Figure 5 shows the I-V curves of p-Si/Pt and p-Si/n-Si/Pt along with Bi_2WO_6/Co-Pi and WO_3 photoanode. We confirmed that the measured operating photocurrent using the combination of a photocathode and a photoanode was well matched with the cross point in the I-V curves.

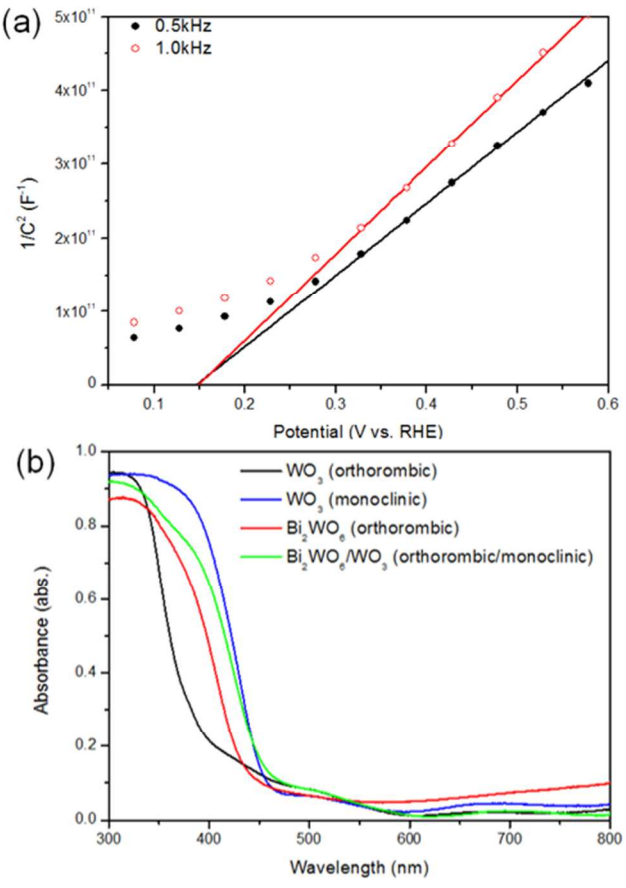

Figure 4. (a) Characterization of a flat-band potential of the Bi_2WO_6 photoanode samples by Mott-Schottky plots, and (b) UV-vis absorption spectra of various photoanode

Figure 5. (a) I-V curves of photocathodes and photoanodes which show lowering the onset potential of the photoanode contributes the enhanced operating current

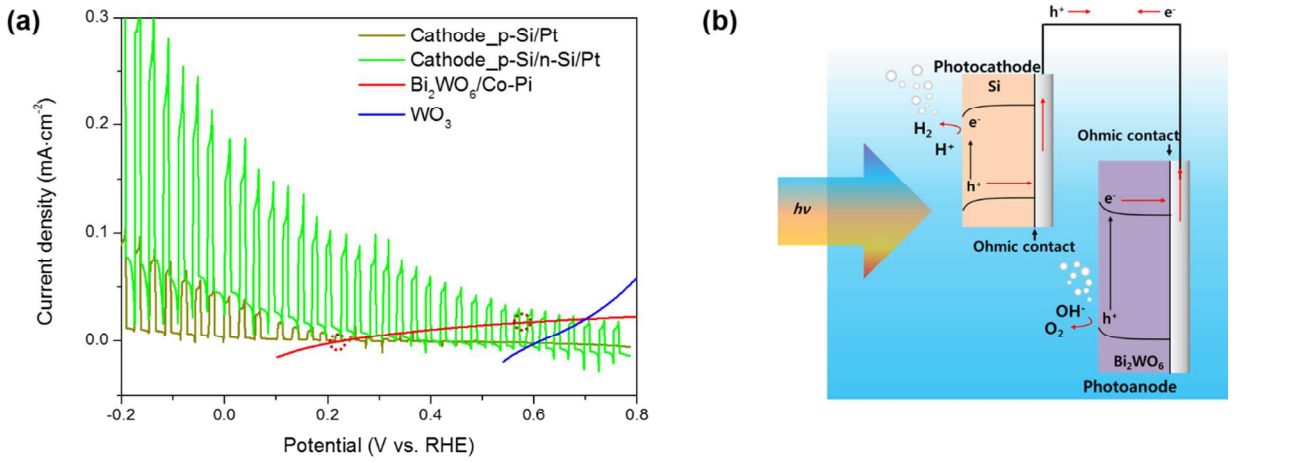

with the combination of a silicon photocathode. (b) Schematic diagram of a p/n photodiode PEC cell composed of a silicon photocathode and a Bi_2WO_6 photoanode illustrating the overall water splitting

When Bi_2WO_6/Co-Pi was combined with p-Si/Pt, the operating current was 3 μA/cm^2 without any external bias potentials while no photocurrent was observed when WO_3 was combined. Again, when p-Si/n-Si/Pt was linked with Bi_2WO_6/Co-Pi, the photocurrent was enhanced to 20 μA/cm^2 which is a higher value compared to the case using WO_3. Bi_2WO_6/Co-Pi photoanode in the present work resulted in the higher operating current although its maximum photocurrent level is much lower than that of WO_3 photoanode,[8] which shows the importance of controlling onset potentials of the photoelectrodes in p/n PEC cells. Here, lowering the onset potential of Bi_2WO_6 provides the opportunity for efficient spontaneous water splitting in a composite PEC system. The poor photocurrent is expected to increase upon improving the electrical properties of Bi_2WO_6.

4. Conclusions

We demonstrated the growth of Bi2WO6 nanostructures on an FTO substrate via a two-step hydrothermal synthesis during which WO3 0.33 H2O nanorods on the FTO substrate convert to orthorhombic Bi2WO6. The effect of the annealing temperatures on the photoanodic activities of Bi2WO6 was monitored, and 600 °C is the optimum annealing temperature. A three-fold improvement in the photocurrent occurs upon coating the surface of the nanostructured Bi2WO6 photoanode with an OER catalyst, i.e., Co-Pi. In the present work, hydrothermally prepared Bi2WO6 has a lower onset potential (0.15 V vs. RHE) than other metal-oxide semiconductors, such as WO3 and Fe2O3 as a result of shifting the CB to a higher level. Although the photocurrent level of Bi2WO6 requires further improvement, its low onset potential is promising for the realization of spontaneous water splitting in composite systems, such as p/n photodiodes or PV cell-combined tandem cells.

Acknowledgements

This research was funded by the institutional program of Korea Institute of Science and Technology (KIST).

Notes and references

[a]Clean Energy Research Center, Korea Institute of Science and Technology (KIST), Hwarangno 14-gil 5, Seounbuk-gu, Seoul 136-791, Republic of Korea.
[b]Department of Chemistry, College of Science, Korea University, Anam Dong, Seoul 136-713, Republic of Korea.
[c] Department of Clean Energy and Chemical Engineering, Korea University of Science and Technology, Daejeon 305-350, Republic of Korea

E-mail: yjhwang@kist.re.kr, (Yun Jeong Hwang), and joocat@kist.re.kr (Oh-Shim Joo)

† Footnotes should appear here. These might include comments relevant to but not central to the matter under discussion, limited experimental and spectral data, and crystallographic data.
Electronic Supplementary Information (ESI) available: [details of any supplementary information available should be included here]. See DOI: 10.1039/c000000x/

1. T. A. Faunce, W. Lubitz, A. W. Rutherford, D. MacFarlane, G. F. Moore, P. Yang, D. G. Nocera, T. A. Moore, D. H. Gregory, S. Fukuzumi, K. B. Yoon, F. A. Armstrong, M. R. Wasielewski and S. Styring, *Energy Environ. Sci.*, 2013, **6**, 695.
2. 1st UK Solar to Fuels Symposium, London UK, January, 2012.
3. M. Gratzel, *Nature*, 2001, **414**, 338.

4. Z. Chen, T. F. Jaramillo, T. G. Deutsch, A. Kleiman-Shwarsctein, A. J. Forman, N. Gaillard, R. Garland, K. Takanabe, C. Heske, M. Sunkara, E. W. McFarland, K. Domen, E. L. Miller, J. A. Turner and H. N. Dinh, *J. Mater. Res.*, 2010, **25**, 3.
5. I. S. Cho, Z. Chen, A. J. Forman, D. R. Kim, P. M. Rao, T. F. Jaramillo and X. Zheng, *Nano Lett.*, 2011, **11**, 4978.
6. M. Ni, M. K. H. Leung, D. Y. C. Leung and K. Sumathy, *Renewable Sustainable Energy Rev.*, 2007, **11**, 401.
7. M. Higashi, R. Abe, T. Takata and K. Domen, *Chem. Mater.*, 2009, **21**, 1543.
8. S. S. Kalanur, Y. J. Hwang, S. Y. Chae and O. S. Joo, *J. Mater. Chem. A*, 2013, **1**, 3479.
9. S. C. Warren, K. Voïtchovsky, H. Dotan, C. M. Leroy, M. Cornuz, F. Stellacci, C. Hébert, A. Rothschild and M. Grätzel, *Nat. Mater.*, 2013, **12**, 842.
10. K. Sivula, F. Le Formal and M. Grätzel, *ChemSusChem*, 2011, **4**, 432.
11. K. Sivula, F. L. Formal and M. Grätzel, *Chem. Mater.*, 2009, **21**, 2862.
12. K. Maeda and K. Domen, *J. Phys. Chem. Lett.*, 2010, **1**, 2655.
13. B. D. Alexander, P. J. Kulesza, I. Rutkowska, R. Solarska and J. Augustynski, *J. Mater. Chem.*, 2008, **18**, 2298.
14. J. C. Hill and K.-S. Choi, *J. Mater. Chem. A*, 2013, **1**, 5006.
15. L. Zhang, C. Baumanis, L. Robben, T. Kandiel and D. Bahnemann, *Small*, 2011, **7**, 2714.
16. L. Zhang and D. Bahnemann, *ChemSusChem*, 2013, **6**, 283.
17. Y. Zhang, N. Zhang, Z.-R. Tang and Y.-J. Xu, *Chem. Sci.*, 2013, **4**, 1820.
18. J. Tian, Y. Sang, G. Yu, H. Jiang, X. Mu and H. Liu, *Adv. Mater.*, 2013, **25**, 5075.
19. A. Kudo and S. Hijii, *Chem. Lett.*, 1999, **28**, 1103.
20. X. Ding, Z. H. Ai and L. Z. Zhang, *J. Hazard. Mater.*, 2012, **239**, 233.
21. L. W. Zhang, Y. J. Wang, H. Y. Cheng, W. Q. Yao and Y. F. Zhu, *Adv. Mater.*, 2009, **21**, 1286.
22. S. M. Sun, W. Z. Wang and L. Zhang, *J. Phys. Chem. C*, 2012, **116**, 19413.
23. D. K. Ma, S. M. Huang, W. X. Chen, S. W. Hu, F. F. Shi and K. L. Fan, *J. Phys. Chem. C*, 2009, **113**, 4369.
24. C. Ng, A. Iwase, Y. H. Ng and R. Amal, *J. Phys. Chem. Lett.*, 2012, **3**, 913.
25. M. W. Kanan and D. G. Nocera, *Science*, 2008, **321**, 1072.
26. F. F. Abdi and R. van de Krol, *J. Phys. Chem. C*, 2012, **116**, 9398.
27. Y. L. Kawamura, T. Sakka and Y. H. Ogata, *J. Electrochem. Soc.*, 2005, **152**, C701.
28. S. W. Boettcher, E. L. Warren, M. C. Putnam, E. A. Santori, D. Turner-Evans, M. D. Kelzenberg, M. G. Walter, J. R. McKone, B. S. Brunschwig, H. A. Atwater and N. S. Lewis, *J. Am. Chem. Soc.*, 2011, **133**, 1216.
29. K. Goto, T. Kawashima and N. Tanabe, *Sol. Energy Mater. Sol. Cells*, 2006, **90**, 3251.
30. F. F. Abdi, L. Han, A. H. M. Smets, M. Zeman, B. Dam and R. van de Krol, *Nat. Commun.*, 2013, **4**.
31. M. G. Walter, E. L. Warren, J. R. McKone, S. W. Boettcher, Q. Mi, E. A. Santori and N. S. Lewis, *Chem. Rev.*, 2010, **110**, 6446.
32. M. F. Weber and M. J. Dignam, *J. Electrochem. Soc.*, 1984, **131**, 1258.
33. Y. Hou, B. L. Abrams, P. C. K. Vesborg, M. E. Björketun, K. Herbst, L. Bech, A. M. Setti, C. D. Damsgaard, T. Pedersen, O. Hansen, J. Rossmeisl, S. Dahl, J. K. Nørskov and I. Chorkendorff, *Nat. Mater.*, 2011, **10**, 434.

